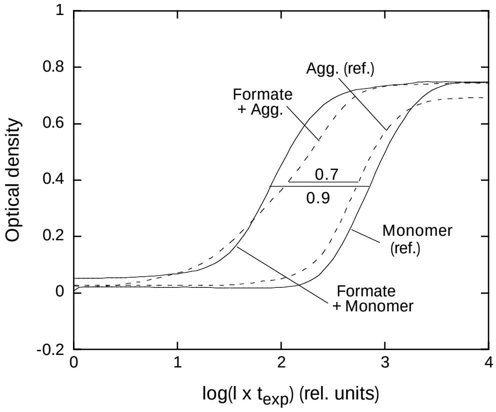

Figure 4 Effect of formate doping on the sensitivity of AgBr emulsions sensitized with carbocyanine dye. After the precipitation and doping (10^{-6} mol $HCOO^-$/mol Ag^+) by formate as in Fig. 2, the AgBr crystals were sensitized by the dye (3-(2-(3-(5-chloro-3-(3-sodium-sulpho-propyl)-benzoxazol-2-yl)-2-ethyl-allylidene)-5-chloro-benzoxazolium-3-yl)-propane-1-sulphonic acid betaine) in the monomeric form ($\lambda_{max} = 480$ and 500 nm, surface coverage = 0.2) and excited at $\lambda_{exp} \geqslant 477$ nm, or in the J-aggregate form (additional λ_{max} at 552 nm, surface coverage = 0.8) and excited at $\lambda_{exp} \geqslant 519$ nm. Development by M-AA-1 is delayed for 20 min, after $t_{exp} = 10^{-2}$ s.

also be transferred from the highest occupied molecular orbital (HOMO) of the dye to the Fermi level of the dopant formate, so blocking electron–hole recombination[3]. Our results from emulsions sensitized by a carbocyanine thought to fulfill the above criterion indicate that the sensitivity is indeed increased (Fig. 4), compared to emulsions without formate supposed to absorb the same quantity of photons. Depending on the surface coverage by dye molecules, these are in the form of either monomers or J-aggregates, which are two-dimensional arrays of edged-on adsorbed dye molecules with a large slip angle. The difference is about $\Delta\log(I \times t_{exp}) = 0.9$ for emulsions sensitized by dye monomers ($\lambda_{max} = 480$ and 500 nm), excited at $\lambda_{exp} \geqslant 477$ nm; for emulsions sensitized by J-aggregates (additional λ_{max} at 552 nm), excited at $\lambda_{exp} \geqslant 519$ nm, we obtain $\Delta\log(I \times t_{exp}) = 0.7$. This enables us to assess the effect of aggregates only without coexisting monomers. The sensitivity enhancement that is systematically observed in the presence of formate ion therefore attests to efficient hole transfer to the dopant formate from the HOMO level of the dye, in both the monomer and the J-aggregate forms. This mechanism is comparable with the scavenging of the intrinsic hole created by direct AgBr excitation, and results in a marked inhibition of recombination. ☐

Received 22 September; accepted 18 October 1999.

1. Harbison, J. M. & Spencer, H. E. in *The Theory of the Photographic Process* 4th edn (ed. James, T. H.) (Macmillan, New York, 1977).
2. Glafkides, P. *Chimie et Physique Photographiques* 5th edn (CEP Edition, Paris, 1987).
3. Tani, T. *Photographic Sensitivity* (Oxford Univ. Press, New York, 1995).
4. Hamilton, J. F. & Baetzold, R. C. The paradox of Ag_2 centers on AgBr: reduction sensitization vs. photolysis. *Photogr. Sci. Eng.* **25,** 189–196 (1981).
5. Tani, T. & Murofishi, M. Silver microclusters on silver halide grains as latent image and reduction sensitization centers. *J. Imaging Sci. Technol.* **38,** 1–9 (1994).
6. Hailstone, R. K. *et al.* Achieving high quantum sensitivities with hydrogen hypersensitization. 1. Measurement. *J. Imaging Sci.* **32,** 113–124 (1988).
7. De Keyzer, R., Tréguer, M., Belloni-Cofler, J. & Remita, H. (AGFA-Gevaert) A photosensitive silver halide element with increased photosensitivity. *Patent no.* EP97 202.897.0 (11 December 1997).
8. Hailstone, R. K., Liebert, N. B., Levy, M. & Hamilton, J. F. Latent subimage in a AgBr model emulsion. 1. Sulfur-plus-gold-sensitized versions. *J. Imaging Sci.* **31,** 185–193 (1987).
9. Schwarz, H. A. & Dodson, R. W. Reduction potentials of CO_2^- and the alcohol radicals. *J. Phys. Chem.* **93,** 409–414 (1989).
10. Allen, A. O. *The Radiation Chemistry of Water and Aqueous Solutions* (Van Nostrand, Princeton, 1961).
11. Belloni, J., Saito, E. & Tissier, F. Photodetachment of electrons from alcoholate ions in liquid ammonia. *J. Phys. Chem.* **79,** 308–309 (1975).
12. Swallow, A. J. in *The Study of Fast Processes and Transient Species by Electron Pulse Radiolysis* (eds Baxendale, J. H. & Busi, F.) 289–315 (NATO ASI Ser. Vol. 86, Reidel, Dordrecht, 1981).
13. Frank, S. N. & Bard, A. J. Semiconductor electrodes. 12. Photoassisted oxidations and photoelectrosynthesis at polycrystalline TiO_2 electrodes. *J. Am. Chem. Soc.* **99,** 4667–4675 (1977).
14. Hykaway, N., Sears, W. M., Morisaki, H. & Morrison, S. R. Current-doubling reactions on titanium dioxide photoanodes. *J. Phys. Chem.* **90,** 6663–6667 (1986).
15. Herz, A. H., Danner, R. & Janusonis, G. in *Absorption from Aqueous Solution* 173 (American Chemical Soc., Washington DC, 1968).
16. Guo, S. & Hailstone, R. Spectroscopic and sensitometric studies of chemically produced silver clusters. *J. Imaging Sci. Technol.* **40,** 210–219 (1996).
17. Mostafavi, M., Marignier, J.-L., Amblard, J. & Belloni, J. Nucleation dynamics of silver aggregates. Simulation of the photographic development process. *Rad. Phys. Chem.* **34,** 605–617 (1989).
18. Belloni, J., Mostafavi, M., Marignier, J-L. & Amblard, J. Quantum size effects and photographic development. *J. Imaging Sci.* **35,** 68–74 (1991).
19. Hailstone, R. K. Liebert, N. B., Levy, M. & Hamilton, J. F. Achieving high quantum sensitivities with hydrogen hypersensitization. 2. Mechanism. *J. Imaging Sci.* **35,** 219–230 (1991).
20. Silberstein, L. On the number of quanta required for the developability of a silver halide grain. *J. Opt. Soc. Am.* **31,** 343–348 (1941).

Acknowledgements

The present work has been performed under an AGFA–CNRS contract.

Correspondence and requests for materials should be addressed to J.B. (e-mail: jacqueline.belloni@lpcr.u-psud.fr).

Periodic mesoporous organosilicas with organic groups inside the channel walls

Tewodros Asefa, Mark J. MacLachlan, Neil Coombs & Geoffrey A. Ozin

Materials Chemistry Research Group, Department of Chemistry,
80 St George Street, University of Toronto, Toronto, Ontario, Canada M5S 3H6

Surfactant-mediated synthesis methods have attracted much interest for the production of inorganic mesoporous materials, which can, on removal of the surfactant template, incorporate polymeric, organic, inorganic and organometallic 'guests' in their pores[1,2]. These materials—initially made of silica[3–5], but now also available in the form of other oxides[6–9], sulphides[10,11], phosphates[12] and metals[13]—could find application in fields ranging from catalysis, adsorption and sensing technology to nanoelectronics. The extension of surfactant-mediated synthesis to produce inorganic–organic hybrid material (that is, materials that contain organic groups as an integral part of their framework structure) promises access to an even wider range of application possibilities. Such hybrid materials have been produced in the form of amorphous silicates (xerogels) that indeed display unique properties different to those of the individual components[14–20], but their random networks with broad pore-size distributions severely limit the shape and size selectivity of these materials. Mesoporous hybrid materials with periodic frameworks have been synthesized, but the organic groups are all terminally bonded to the pore surface, rather than incorporated into the pore walls[21–26]. Here we describe a periodic mesoporous organosilica containing bridge-bonded ethene groups directly integrated into the silica framework. We are able to solvent-extract and ion-exchange the surfactant templates to create a stable and periodic mesoporous ethenesilica with high surface area and ethene groups that are readily accessible for chemical reaction. Recent syntheses of similar periodic mesoporous organosilicas[27,28] and the ability to incorporate a variety of bridging organic and organometallic species raise the prospect of being able to fuse organic synthesis and inorganic materials chemistry to generate new materials with interesting chemical, mechanical electronic, optical and magnetic properties.

In a typical synthesis, a mixture of bis(triethoxysilyl)ethene (BTE) and tetraethylorthosilicate (TEOS) was added to a solution of cetyltrimethylammonium bromide (CTABr), NH_4OH and H_2O. Samples were prepared containing BTE:TEOS in mole fractions of 1:0 (BTE100), 0.75:0.25 (BTE75), 0.50:0.50 (BTE50), 0.25:0.75

(BTE25) and 0:1 (BTE0) based on Si contribution. After ageing for 4 days, the products were isolated and washed carefully with water. The surfactant was removed from the pores by mild solvent extraction or ion exchange that leave intact the mesopores and the framework. After a single extraction, the amount of surfactant collected was ~30 wt% of the initial material.

To prove that the ethene moiety was incorporated into the material as a bridge-bonded group, and that the materials were well-ordered and mesoporous, a series of samples was examined by powder X-ray diffraction, transmission electron microscopy (TEM), FT-Raman spectroscopy, ^{1}H magic angle spinning (MAS) NMR, ^{13}C and ^{29}Si cross-polarization (CP) MAS NMR spectroscopies, differential thermogravimetric analysis (DTGA), and N_2 gas adsorption (see Figs 5–11 in Supplementary Information).

Powder X-ray diffraction patterns for as-synthesized samples containing different proportions of BTE to TEOS are shown in Fig. 1a. Four peaks were observed for samples BTE50, BTE25 and BTE0, which could be indexed as the (100), (110), (200) and (210) reflections of a hexagonal symmetry lattice with a unit cell dimension $a \approx 47$ Å (see Figs 6 and 7 in Supplementary Information). Samples BTE100 and BTE75 showed the (100) diffraction peak, but the other three peaks were less intense. These results suggest the presence of a periodic arrangement of channels in a hexagonal geometry. We note that the intensities of the peaks become less intense as the relative amount of BTE to TEOS increases. As more SiO_2 is replaced with ethene groups, the electron density of the framework decreases relative to that of the surfactant-containing pores. Moreover, removing surfactant from the pores increases the electron density of the framework relative to the pores[29], and increases the intensity of the diffraction pattern for all samples (Fig. 1b). Together these data demonstrate that ethene functionality has been incorporated into the framework of the periodic mesoporous silica.

TEM images of the materials are consistent with the powder X-ray diffraction results, showing hexagonal symmetry mesopores throughout the sample and a pore centre-to-centre distance of ~45–50 Å (Fig. 1c–e). The TEM image of as-synthesized BTE100 (Fig. 1c) shows that the material is as well ordered as BTE0 (MCM-41), even though a slight difference between their powder X-ray diffraction patterns was observed (see Fig. 8 in Supplementary Information). The quality of the hexagonal mesostructure is retained following a series of surfactant extractions (Fig. 1d). A TEM image of twice-extracted BTE100 viewed parallel to the channel axis is displayed in Fig. 1e.

Figure 2 shows DTGA traces of as-synthesized and solvent-extracted (once and twice) BTE100, and as-synthesized BTE0. A small mass loss of adsorbed water occurs in the range 40–80 °C. A weight loss of ~30% between 150 and 350 °C corresponds to surfactant and some ethene. ^{13}C CP-MAS NMR of a sample of BTE100, calcined in air at 350 and 400 °C for 6 hours, showed complete loss of surfactant and some ethene at 350 °C with complete removal of ethene by 400 °C. Variable-temperature powder X-ray diffraction (room temperature to 1,000 °C) showed a decrease of ~10 Å in the d_{100} spacing of BTE100, roughly twice that of BTE0 despite similar initial unit-cell dimensions. This distinction probably

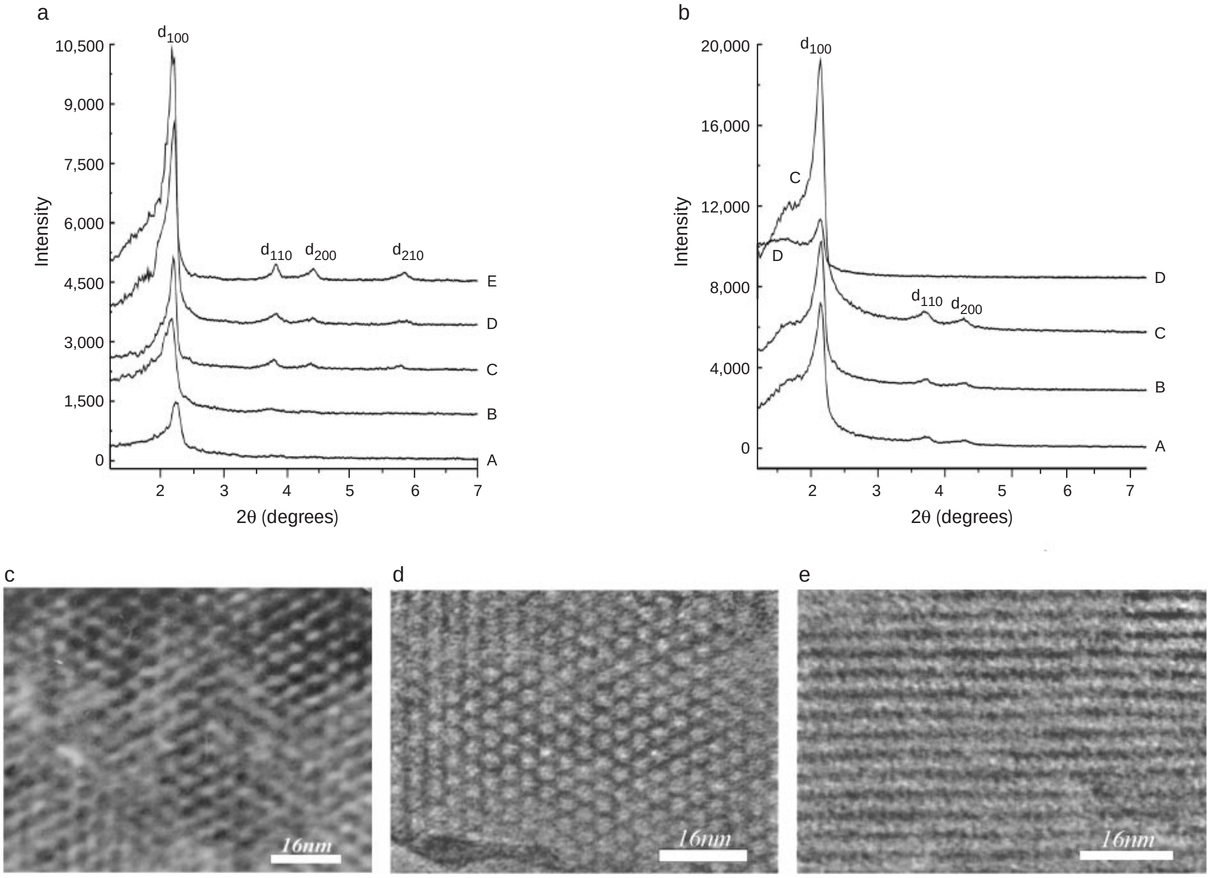

Figure 1 Powder X-ray diffraction patterns and TEM images of mesoporous ethenesilica. (See Figs 6–8 in Supplementary Information.) **a**, Powder X-ray diffraction (PXRD) patterns for as-synthesized samples containing different proportions of BTE and TEOS. Shown are the diffraction patterns for BTE100 (trace A), BTE75 (B), BTE50 (C), BTE25 (D) and BTE0 (E). The patterns confirm the hexagonal symmetry of the materials. **b**, Comparison of PXRD patterns of BTE100; after solvent-extraction (trace A), after ion-exchange (B), after additional solvent-extraction (C), and as-synthesized (D). The (110) and (200) reflections are clearly visible after the surfactant was extracted. **c**, **d**, TEM images of the well-ordered hexagonal mesostructure of BTE100 as-synthesized and after two solvent-extractions, respectively. **e**, View parallel to the channel axis of the BTE100 sample (twice solvent-extracted). PXRD patterns were measured with a Siemens D5000 diffractometer using Ni-filtered Cu-Kα radiation with $\lambda = 1.54178$ Å. TEM images were recorded on a Philips 430 microscope operating at an accelerating voltage of 100 kV.

arises from the 'elastic response' of the channels to loss of ethene from the silica walls. The mesostructure of BTE100 is maintained to over 1,000 °C, well after the ethene groups have been eliminated from the framework. This implies that the material 'healed' during the thermal elimination of the ethene moiety via condensation of silanol groups.

FT-Raman spectroscopy showed the presence of the ethene groups in as-synthesized and solvent-extracted samples (Fig. 3a, b). A spectrum for ion-exchanged BTE100 is shown in Fig. 3c. A C=C stretching mode at 1,580 cm^{-1}, absent in BTE0, remains after surfactant extraction. Its intensity increases with the amount of BTE in the framework. Bands around 2,800–3,200 cm^{-1} and 1,300 cm^{-1} are assigned to C–H stretching and C–H deformation modes of the surfactant and ethene groups.

Confirmation of incorporation of ethene groups directly inside the framework was obtained by NMR spectroscopy. The ^{1}H MAS NMR spectra of as-synthesized, solvent-extracted and ion-exchanged BTE100 samples are shown in Fig. 4a. Each sample shows a resonance at ~2 p.p.m. due to alkyl hydrogens of the surfactant, which decreases after surfactant extraction. Peaks at ~4 and 7 p.p.m. are attributed to silanol and ethene hydrogens, respectively. Upon solvent extraction, the ratio of silanol : ethene proton resonances increases, consistent with the replacement of cationic surfactants with protons to form silanol groups. ^{13}C CP-MAS NMR shows a resonance at 144 p.p.m. attributed to ethene carbons, and resonances below 70 p.p.m. correspond to the carbons of the surfactant (Fig. 4b). An increase in ethene : surfactant intensity was observed after samples underwent solvent extraction and ion exchange.

^{29}Si CP-MAS NMR of as-synthesized samples show mostly T_3 (C=C)-*Si*-$(OSi)_3$ sites and some T_2(C=C)-*Si*-$(OSi)_2$(OH) sites at approximately −83 and −73 p.p.m., respectively (Fig. 4c). For comparison, Q_4 *Si*-$(OSi)_4$ and Q_3 (HO)-*Si*-$(OSi)_3$ sites of mesoporous silica (BTE0) were observed at −111 and −102 p.p.m., respectively. After solvent-extraction an increase in T_2, and the appearance of a small amount of T_1 (C=C)-*Si*-(OSi)$(OH)_2$ (about −64 p.p.m.) were observed as silanols replaced surfactants (see Figs 10, 11 in Supplementary Information). Minor Q_3 (−101 p.p.m.) and Q_4(−111 p.p.m.) sites were seen after surfactant extraction. They probably arise from slight hydrolysis of ethene–silicon bonds[30,31]. Spectra obtained without CP showed similar results.

Nitrogen adsorption isotherms (obtained at 77 K) for BTE100 materials that had been once, twice and thrice solvent-extracted and then vacuum thermally treated were all found to be type IV, which is characteristic of a mesoporous silica material. Analysis of the isotherms for the three samples yielded an average BET surface area of 637 ^{2} g^{-1}, a pore volume of 0.60 cm^3 g^{-1} and a pore diameter of 39.4 Å (see Fig. 9 in Supplementary Information). With the unit-cell size of 47 Å, determined from powder X-ray diffraction, this yields a channel wall thickness of 7–8 Å.

To demonstrate the chemical accessibility of ethene groups, bromination of the ethene groups in BTE100 samples was attempted (see Fig. 5 in Supplementary Information). The sample

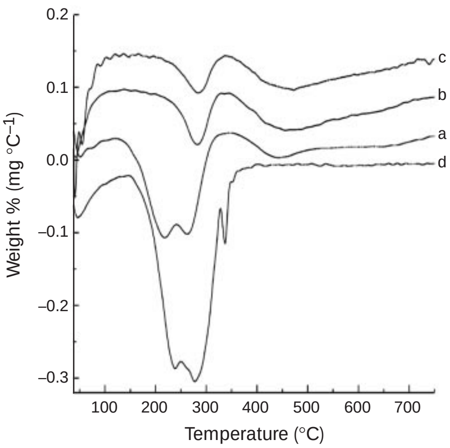

Figure 2 Differential thermogravimetric analysis (DTGA) of mesoporous ethenesilica. Traces a–c, results for BTE100; as-synthesized (trace a), once solvent-extracted (b) and twice solvent-extracted (c). Trace d, as-synthesized BTE0 (MCM-41). A transition around 80 °C corresponds to desorption of water from the channels. A second transition occurring between 150 and 250 °C corresponds to removal of most of the surfactant (space filling) in the material. A third transition occurring between 250 and 350 °C corresponds to the loss of the remaining surfactant (charge balancing) and the loss of some of the ethylene groups. Solid-state NMR of samples calcined at 400 °C did not show any trace of surfactant or ethylene groups, whereas samples calcined at 350 °C showed ethylene and trace amounts of surfactant. In samples containing BTE, a weight loss beyond 350 °C is attributed to loss of some ethylene groups and to loss of water, due to condensation of silanol groups. DTGA data were obtained at a heating rate of 5 °C min^{-1} under a flow of N_2 on a Perkin-Elmer TGA7 instrument.

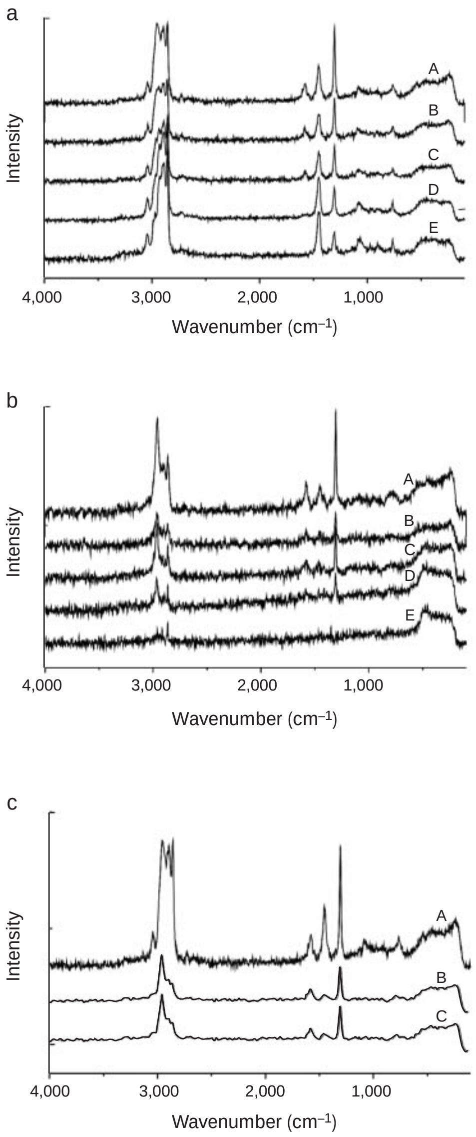

Figure 3 Raman spectra of mesoporous ethenesilica. **a**, **b**, As-synthesized and solvent-extracted samples, respectively. Each panel shows five spectra: trace A, BTE100; B, BTE75; C, BTE50; D, BTE25; E, BTE0. **c**, Spectra of BTE100: A, as-synthesized; B, after solvent-extraction; C, after ion-exchange. After solvent-extraction and ion exchange, all surfactant peaks disappeared while peaks assigned to ethylene groups remained. Raman spectra of the samples were collected using a Bomens MB-158 Fourier transform (FT) Raman spectrometer with an InGaAS near-IR detector and a Spectra Physics Diode Nd:YLF laser emitting at a wavelength of 1,064 nm and at a 350-kHz repetition rate.

was treated in refluxing CH_2Cl_2/Br_2 for 8 days. ^{13}C CP-MAS NMR of the product confirmed that the O_3Si-*CH*=*CH*-SiO_3 groups were entirely consumed during the bromination step. The peak originally observed at 147 p.p.m. was replaced with one at 12 p.p.m. In the ^{29}Si NMR spectrum, the T_2 and T_3 resonances at −73 and −83 p.p.m. for BTE100 were now observed at −58 and −66 p.p.m., respectively. Importantly, no Q_3 or Q_4 environments were observed by ^{29}Si MAS NMR, indicating that Si–C bonds were not cleaved during the reaction. FT-Raman also supported this result, showing elimination of the C=C stretching mode at 1,580 cm^{-1} and appearance of new peaks assigned to C–C and C–Br stretching modes. Powder X-ray diffraction and TEM images of the samples showed that the structural integrity and order of the material is well maintained. On reaction, the hexagonal unit cell of the mesoporous material expanded by 8%, which suggests that these materials may have unusual mechanical properties. This expansion is consistent with the transformation from sp^2 to sp^3 hybridization at the framework C atoms, and the concomitant lengthening of the C–C bond. Adsorption analysis showed a decrease in the BET surface area, pore volume and diameter from 637 $m^2 g^{-1}$, 0.60 $cm^3 g^{-1}$, 39.4 Å to 520 $m^2 g^{-1}$, 0.46 $cm^3 g^{-1}$, 35.6 Å. Chemical analysis of the sample indicated that it contained less bromine than expected for 100% bromination. It appears that while some ethene groups (~10%) were brominated, others reacted with the solvent to form ethane bridges. Nonetheless, these results show that ethene groups incorporated into the channel walls are accessible for chemistry.

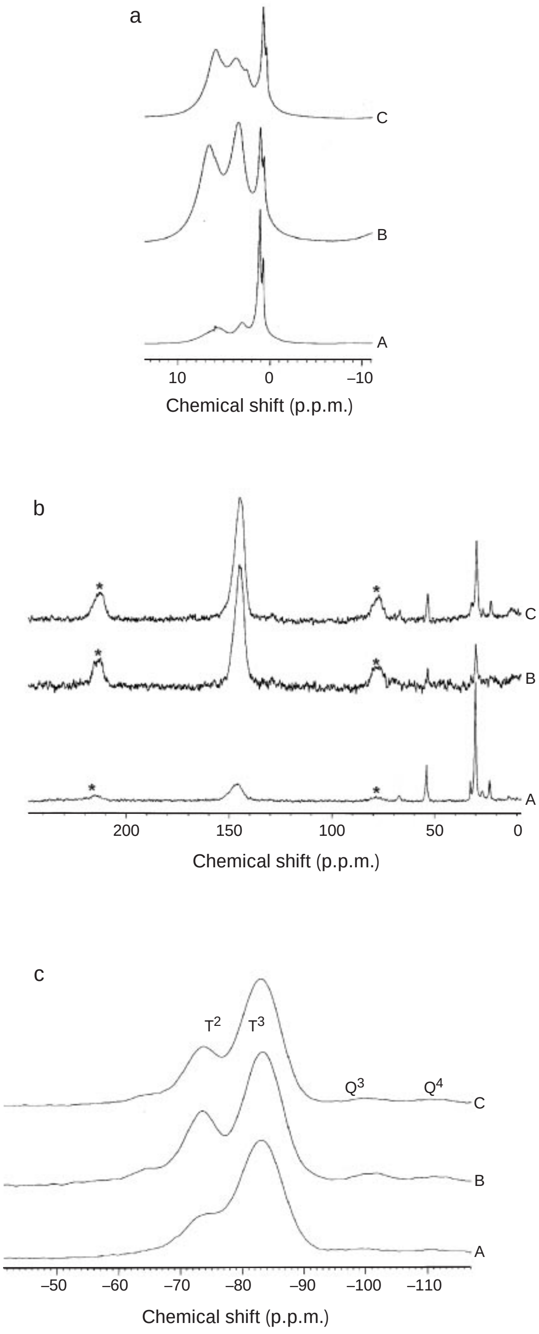

Figure 4 Solid-state NMR spectra of mesoporous ethenesilica, BTE100. (See Figs 10, 11 in Supplementary Information.) **a**, ^1H MAS NMR spectra (3 s recycle delay, 10 scans): trace A, as-synthesized; B, solvent-extracted; and C, ion-exchanged. **b**, ^{13}C CP-MAS NMR spectra (5 ms contact time; 3 s recycle delay; 1,600 scans): trace A, as-synthesized; B, solvent-extracted; and C, ion-exchanged. Both the ^1H and ^{13}C spectra show the disappearance of alkyl groups as the surfactant is extracted leaving the ethylene groups in the materials. Some residual surfactant was also present in the spectrum. **c**, ^{29}Si CP-MAS NMR spectra (10 ms contact time; 4 s recycle delay; 20,000 scans): trace A, as-synthesized; B, solvent-extracted; and C, ion-exchanged. The ^1H (400.1 MHz), ^{13}C CP-MAS (100.6 MHz) and ^{29}Si CP-MAS (79.5 MHz) spectra were obtained with a Bruker DSX400 spectrometer. Samples were spun at a rate of ~6.8 kHz, except for trace A in **a**, which was spun at 6 kHz.

We now compare these periodic mesoporous organosilicas, containing organic groups inside the walls of mesoporous silica, with mesoporous silica containing tethered vinyl groups inside the channels[21]. While both offer the possibility of functionalization and coordinating species, such as catalysts, there are inherent differences between the two classes. The terminal vinyl groups occupy space inside the channels, which may interfere with adsorption of species. There is also a limit of ~25% loading of terminal vinyl groups in the mesoporous silica before structural order is lost. Also, the reactivity of a bridging ethene that is housed within the silica framework, and attached to two electron-withdrawing O_3Si framework moieties, is expected to be different from that of a terminal vinyl located in the channel space and attached to one O_3Si group. Perhaps the most important difference is that chemical reaction of the organic materials in our materials will result in changes to the properties of the framework. If this process can be extended to conducting or semiconducting materials, the creation of a new generation of chemical sensors, membranes and chemical delivery systems may be facilitated. ☐

Methods

General synthesis

A typical synthesis procedure required a mole ratio of 1.00 Si : 114 H_2O : 8.0 NH_4OH (35 wt%) : 0.12 CTABr. BTE and TEOS were used as the silica source. BTE (Gelest) was used without further purification. Samples were prepared with BTE : TEOS in Si mole ratios of 1 : 0 (BTE100), 0.75 : 0.25 (BTE75), 0.50 : 0.50 (BTE50), 0.25 : 0.75 (BTE75) and 0 : 1 (BTE0). CTABr (0.21 g) was added to a solution of NH_4OH (4.43 g, 30 wt%) and deionized water (8.35 g), and the solution was stirred for 30 min in a closed polyethylene bottle. A mixture of BTE : TEOS corresponding to the mole fraction given above, with a total of 4.8 mmol Si (for example, 0.635 g (1.8 mmol) BTE + 0.250 g (1.2 mmol) TEOS for sample BTE75), was slowly added to the base/surfactant solution with slow stirring. After stirring for 30 min, the solutions were aged at 80 °C for 4 d in closed polyethylene bottles. The white powder was collected by filtration, washed thoroughly with water, and air-dried under ambient conditions. A typical yield was 0.690 g for BTE75. BET surface area measurements were obtained for the solvent-extracted samples at McMaster University Powder Processing Facility.

Surfactant removal

Solvent extraction of surfactant was carried out by the procedure of Stein *et al.*[21] An as-synthesized sample (0.5 g) was stirred for 48 h in a refluxing solution of 10 g HCl (36 wt%) and 70 g of methanol. For ion exchange of the surfactant, the sample was stirred in a refluxing solution of 1 g NaCl and 100 g of ethanol.

Bromination

A solvent-extracted sample (0.50 g) was kept under vacuum at 150 °C for 2 d, and then treated in refluxing Br_2/CH_2Cl_2 solution (7.0 g Br_2 + 150 ml CH_2Cl_2) for 8 d. The product was isolated on a Buchner funnel and washed with dichloromethane. Bromine analysis confirmed that Br was incorporated into the mesostructure, though less than the amount expected for an ideal formula of $(CHBr)SiO_{1.5-\frac{x}{2}}(OH)_x$. As we have shown that all of the ethene groups were consumed, some may have reacted with the solvent. We are investigating the mechanism of the bromination reaction.

Received 26 July; accepted 1 December 1999.

1. Moller, K. & Bein, T. Inclusion chemistry in periodic mesoporous hosts. *Chem. Mater.* **10,** 2950–2963 (1998).
2. Ozin, G. A., Chomski, E., Khushalani, D. & MacLachlan, M. J. Mesochemistry. *Curr. Opin. Colloid Interface Sci.* **3,** 181–193 (1998).
3. Kresge, C. T., Leonowicz, M., Roth, W. J., Vartuli, J. C. & Beck, J. C. Ordered mesoporous molecular sieves synthesized by a liquid-crystal template mechanism. *Nature* **359,** 710–712 (1992).
4. Beck, J. S. *et al.* A new family of mesoporous molecular sieves prepared with liquid crystal templates. *J. Am. Chem. Soc.* **114,** 10834–10843 (1992).
5. Attard, G. S., Glyde, J. C. & Goltner, C. G. Liquid-crystalline phases as templates for the synthesis of mesoporous silica. *Nature* **378,** 366–368 (1995).
6. Tian, Z.-R. *et al.* Manganese oxide mesoporous structures: mixed-valent semiconducting catalysts. *Science* **276,** 926–930 (1997).
7. Bagshaw, S. A. & Pinnavaia, T. J. Mesoporous alumina molecular sieves. *Angew. Chem. Int. Edn Engl.* **35,** 1102–1105 (1996).
8. Antonelli, D. M. & Ying, J. Y. Synthesis of a stable hexagonally packed mesoporous niobium oxide molecular sieve through a novel ligand-assisted templating mechanism. *Angew. Chem. Int. Edn Eng.* **35,** 426–430 (1996).
9. Hue, Q. S. *et al.* Generalized synthesis of periodic surfactant/inorganic composite materials. *Nature* **368,** 317–321 (1994).
10. Braun, P. V., Osenar, P. & Stupp, S. I. Semiconducting superlattices templated by molecular assemblies. *Nature* **380,** 325–328 (1996).
11. MacLachlan, M. J., Coombs, N. & Ozin, G. A. Non-aqueous supramolecular assembly of mesostructured metal germanium sulphides from $[Ge_4S_{10}]^{4-}$ clusters. *Nature* **397,** 681–684 (1999).
12. Ciesla, U., Schacht, S., Stucky, G. D., Unger, K. K. & Scüth, F. Formation of a porous zirconium oxophosphate with a high surface area by a surfactant-assisted synthesis. *Angew. Chem. Int. Edn Engl.* **35,** 541–543 (1996).
13. Attard, G. S., Göltner, C. G., Corker, J. M., Henke, S. & Templer, R. H. Liquid-crystal templates for nanostructured metals. *Angew. Chem. Int. Edn Engl.* **36,** 1315–1317 (1997).
14. Dagani, R. Nanocomposites. *Chem. Eng. News* **77**(23), 25–37 (1999).
15. Schubert, U., Hüsing, N. & Lorenz, A. Hybrid inorganic-organic materials by sol-gel processing of organofunctional metal alkoxides. *Chem. Mater.* **7,** 2010–2027 (1995).
16. Corriu, R. J. P. & Leclercq, D. Recent developments of molecular chemistry for sol-gel processes. *Angew. Chem. Int. Edn Engl.* **35,** 1420–1436 (1996).
17. Cerveau, G. & Corriu, R. J. P. Some recent developments of polysilsesquioxanes chemistry for materials science. *Coord. Chem. Rev.* **180,** 1051–1071 (1998).
18. Shea, K. J., Loy, D. A. & Webster, O. Arylsilsesquioxane gels and related materials. New hybrids of organic and inorganic networks. *J. Am. Chem. Soc.* **114,** 6700–6710 (1992).
19. Loy, D. A. & Shea, K. J. Bridged polysilsequioxanes. Highly porous hybrid organic-inorganic materials. *Chem. Rev.* **95,** 1431–1442 (1995).
20. Sellinger, A. *et al.* Continuous self-assembly of organic-inorganic nanocomposite coatings that mimic nacre. *Nature* **394,** 256–260 (1998).
21. Lim, M. H., Blanford, C. F. & Stein, A. Synthesis and characterization of a reactive vinyl-functionalized MCM-41: probing the internal pore structure by a bromination reaction. *J. Am. Chem. Soc.* **119,** 4090–4091 (1997).
22. Fowler, C. E., Lebeau, B. & Mann, S. Covalent coupling of an organic chromophore into functionalized MCM-41 mesophases by template-directed co-condensation. *Chem. Commun.* 1825–1826 (1998).
23. Burkett, S. L., Sim,s S. D. & Mann, S. Synthesis of hybrid inorganic-organic mesoporous silica by co-condensation of siloxane and organosiloxane precursors. *Chem. Commun.* 1367–1368 (1996).
24. Mercier, L. & Pinnavaia, T. J. Access in mesoporous materials: advantages of a uniform pore structure in the design of a heavy metal ion adsorbent for environmental remediation. *Adv. Mater.* **9,** 500–503 (1997).
25. Feng, X. *et al.* Functionalized monolayers on ordered mesoporous supports. *Science* **276,** 923–926 (1997).
26. Van Rhijn, W. M., De Vos, D. E., Sels, B. F., Bossaert, W. D. & Jacobs, P. A. Sulfonic acid functionalised ordered mesoporous materials as catalysts for condensation and esterification reactions. *Chem. Commun.* 317–318 (1998).
27. Inagaki, S., Guan, S., Fukushima, Y., Ohsuna, T. & Terasaki, O. Novel mesoporous materials with a uniform distribution of organic groups and inorganic oxide in their frameworks. *J. Am. Chem. Soc.* **121,** 9611–9614 (1999).
28. Melde, B. J., Holland, B. T., Blanford, C. F. & Stein, A. Mesoporous sieves with unified hybrid inorganic/organic frameworks. *Chem. Mater.* **11,** 3302–3308 (1999).
29. Marler, B., Oberhagemann, U., Vortmann, S. & Gies, H. Influence of the sorbate type on the XRD peak intensities of loaded MCM-41. *Micropor. Mater.* **6,** 375–383 (1996).
30. Chevalier, P., Corriu, R. J. P., Delord, P., Moreau, J. J. E. & Chiman, M. W. Design of porous silica from hybrid organic-inorganic precursors. *New J. Chem.* **22,** 423–433 (1998).
31. Boury, B. *et al.* M. W. Hybrid inorganic–inorganic xerogel access to meso- and microporous silica by thermal and chemical treatment. *Chem. Mater.* **11,** 281–291 (1999).

Supplementary information is available on *Nature*'s World-Wide Web site (http://www.nature.com) or as paper copy from the London editorial office of *Nature*.

Acknowledgements

We thank C. Y-Ishii for technical assistance with the synthesis and characterization of a wide range of periodic mesoporous organosilicas. This work was supported by the Natural Sciences and Engineering Research Council (NSERC) of Canada. M.J.M. was supported by an NSERC post-graduate scholarship (1995–99); G.A.O. thanks the Isaac Walton Killam Foundation for a research fellowship (1995–97).

Correspondence and requests for materials should be addressed to G.A.O. (e-mail gozin@alchemy.chem.utoronto.ca).

Seismic anisotropy of the Earth's inner core resulting from flow induced by Maxwell stresses

Shun-ichiro Karato

Department of Geology and Geophysics, University of Minnesota, Minneapolis, Minnesota 55455, USA

Seismological observations indicate that the inner core of the Earth is elastically anisotropic[1]. Anisotropic structures are likely to be formed by dynamic processes and therefore such observations have the potential to provide constraints on flow in the inner core and on the geodynamo itself. But in addition to the difficulties in estimating the relevant physical properties of iron under inner-core conditions[2–4], even the macroscopic processes responsible for generating seismic anisotropy in this region have yet to be determined[5–9]. As a result, the geodynamic significance of seismic anisotropy in the inner core has remained unknown. Here I propose—based on geodynamic and mineral physics considerations—that flow induced by the stress due to the magnetic field, the Maxwell stress, near the inner-core boundary produces an axisymmetric fabric responsible for the observed seismic anisotropy. The resultant seismic anisotropy reflects the geometry of the magnetic field near the inner-core boundary and therefore seismological observations might provide constraints on the geodynamo. This flow also causes non-uniform release of energy at the inner-core boundary, associated with solidification and melting which may affect the pattern of convection in the outer core.

The seismic anisotropy of the Earth's inner core[1] and the rotation of the inner core with respect to the mantle ("super-rotation")[10,11] suggest that this central portion of our planet is dynamically active. The super-rotation and the observed nearly axisymmetric seismic anisotropy suggest an important interaction between the inner and the outer core. Super-rotation is considered to be due to the interaction between the inner and the outer core through the Maxwell stress[12,13], but there has been no consensus as to the likely macroscopic processes that could cause seismic anisotropy. Here I will review some of the previous models of anisotropy in the inner core, and then show that the Maxwell stress could also play a critical role in the formation of the anisotropic fabric in the inner core that causes seismic anisotropy.

As theoretical analysis indicates an effective draining of possible melt from the inner core[14], the most likely cause of seismic anisotropy in the inner core is the lattice preferred orientation (LPO) of iron. In identifying likely macroscopic processes of anisotropic structure formation by LPO, it is important to appreciate that large-strain deformation and/or the long-term action of stress are needed for the development of significant LPO. A plausible macroscopic process must also explain the nearly axial symmetry of anisotropy.

Some previous studies suggested that deformation-induced fabric (that is, LPO) of iron crystals due to thermal convection is the origin of seismic anisotropy[5,15], in much the same way as in the upper mantle. However, theoretical analysis of the energy budget and heat transfer strongly indicates that thermal convection is unlikely in the inner core, because of a low concentration of heat-generating elements and the efficient thermal conduction[16,17]. Furthermore, the axial symmetry of anisotropy is not readily explained by this model.

An alternative model is the texturing of iron crystals during solidification from the liquid outer core[6,7]. Although this model can explain the axial symmetry of anisotropy, a major problem of this